

Characterizing electron temperature gradient turbulence via numerical simulation

W. M. Nevins

Lawrence Livermore National Laboratory, Livermore, California 94551

J. Candy

General Atomics, San Diego, California 92186

S. Cowley

Department of Physics and Astronomy, UCLA, Los Angeles, California 90095-1547

T. Dannert

Centre de Recherches en Physique des Plasmas (CRPP), Ecole Polytechnique Federale de Lausanne (EPFL), CH-1015 Lausanne, Switzerland

A. Dimits

Lawrence Livermore National Laboratory, Livermore, California 94551

W. Dorland

University of Maryland, College Park, Maryland 20742

C. Estrada-Mila

Department of Mechanical and Aerospace Engineering, UCSD, San Diego, California 92093

G. W. Hammett

Princeton Plasma Physics Laboratory, Princeton, New Jersey 08536

F. Jenko and M. J. Pueschel

Max-Planck Institut für Plasmaphysik, D-85748 Garching, Germany

D. E. Shumaker

Lawrence Livermore National Laboratory, Livermore, California 94551

(Received 8 June 2006; accepted 6 November 2006; published online 20 December 2006)

Numerical simulations of electron temperature gradient (ETG) turbulence are presented that characterize the ETG fluctuation spectrum, establish limits to the validity of the adiabatic ion model often employed in studying ETG turbulence, and support the tentative conclusion that plasma-operating regimes exist in which ETG turbulence produces sufficient electron heat transport to be experimentally relevant. We resolve prior controversies regarding simulation techniques and convergence by benchmarking simulations of ETG turbulence from four microturbulence codes, demonstrating agreement on the electron heat flux, correlation functions, fluctuation intensity, and *rms* flow shear at fixed simulation cross section and resolution in the plane perpendicular to the magnetic field. Excellent convergence of both continuum and particle-in-cell codes with time step and velocity-space resolution is demonstrated, while numerical issues relating to perpendicular (to the magnetic field) simulation dimensions and resolution are discussed. A parameter scan in the magnetic shear, s , demonstrates that the adiabatic ion model is valid at small values of s ($s < 0.4$ for the parameters used in this scan) but breaks down at higher magnetic shear. A proper treatment employing gyrokinetic ions reveals a steady increase in the electron heat transport with increasing magnetic shear, reaching electron heat transport rates consistent with analyses of experimental tokamak discharges. © 2006 American Institute of Physics. [DOI: 10.1063/1.2402510]

I. INTRODUCTION

We present direct numerical simulations of electron temperature gradient (ETG) turbulence that serve to characterize the ETG fluctuation spectrum, establish limits to the validity of the adiabatic ion model often employed in studying ETG turbulence, and support the tentative conclusion that plasma operating regimes exist in which ETG turbulence can produce sufficient electron heat transport to be experimentally relevant. In the electrostatic approximation, the equations describing ETG modes¹⁻⁴ are nearly isomorphic to those de-

scribing ion temperature gradient (ITG) modes when considering ETG turbulence for which $k_{\perp}\rho_i \gg 1$ (where k_{\perp} is the component of the ETG wave number perpendicular to the magnetic field and ρ_i is the ion gyroradius) so that the ion response is adiabatic and $k\lambda_{De} \ll 1$ (where λ_{De} is the electron Debye length) so that space-charge effects can be ignored. This near isomorphism between ITG and ETG turbulence involves exchanging ion scales (ρ_i and the ion thermal velocity, v_{ti}) for the corresponding electron scales (the electron gyroradius, ρ_e and the electron thermal velocity, v_{te}). As a result, the transport associated with ETG turbulence is mea-

sured in electron gyro-Bohms, which, for deuterium plasmas, are 60 times smaller than the ion gyro-Bohms used to calibrate ITG turbulence.

The definition of a gyro-Bohm involves a macroscopic length, taken to be the temperature gradient scale length, L_T , throughout this paper. Hence, $\chi_{GB} \equiv (\rho/L_T)\rho v_{th}$. The ion thermal conductivity observed in numerical simulations of ITG turbulence rarely exceeds two ion gyro-Bohms⁵⁻⁹ and there has been substantial controversy regarding how strong ETG turbulence is and whether it can produce sufficiently large electron thermal transport to be experimentally relevant. Some workers¹⁰⁻¹² have reported relatively low levels of electron thermal transport, while others¹³⁻²⁰ report electron thermal conductivities from microturbulence simulations exceeding ten electron gyro-Bohms. However, all of these previous simulations found significant enhancement of $\chi_e/\chi_{e,GB}$ for ETG relative to the value of $\chi_i/\chi_{i,GB}$ seen in equivalent ITG simulations (the reported value of $\chi_e = 3.2\chi_{e,GB}$ in Refs. 11 and 12 is enhanced by a factor of ~ 4 over the equivalent adiabatic-electron ITG results in Ref. 8). We will show that even an electron thermal conductivity of a few electron gyro-Bohms is sufficient to explain the electron transport in some tokamak discharges.

Some of the differences between ETG simulation results can be explained by differences in the operating point of the background plasma supporting the ETG turbulence. However, many of these simulations¹¹⁻²¹ employed similar operating points—an electron analogue of the Cyclone project's ITG benchmark described in Ref. 8 (but note that Refs. 13–15 excluded trapped electrons by setting the local inverse aspect ratio to zero). Nevins *et al.*²¹ demonstrated that the low level of electron thermal transport (three electron gyro-Bohms) at this operating point reported in Refs. 11 and 12 resulted from excessive discrete particle noise in these particle-in-cell (PIC) simulations of ETG turbulence. To study these issues further, verify that independent simulations can achieve consistent ETG results at the same operating point and numerical resolution, and at the request of the Plasma Science and Advanced Computing Initiative program advisory committee,²² we undertook the ETG benchmarking effort reported in Secs. II–IV.

The work of Nevins *et al.*²¹ and initial efforts by this group demonstrated that the ETG turbulence observed in simulations at the electron analogue of the Cyclone ITG benchmark point⁸ including trapped particles is so violent as to make PIC simulations impractical, while continuum simulations at this operating point are limited by the (nonlinear) Courant condition for the $E \times B$ flow (forcing codes with adaptive integrators to progressively shorter time steps) and often fail to reach a steady state. (The simulations of Refs. 13–15 had trapped particles turned off. This provided a long-wavelength cutoff that helped achieve saturation.) Hence, we have concluded that the electron analogue of the Cyclone ITG benchmark point is not an appropriate operating point for benchmarking simulations of ETG turbulence. We present an alternate ETG benchmark operating point in Sec. II together with linear analysis of ETG instability at this operating point. Convergence tests at this new benchmark point are presented in Sec. III, where we demonstrate excel-

lent convergence in time step and velocity space resolution and investigate issues relating to numerical convergence with respect to the perpendicular (to the magnetic field, \mathbf{B}) size and resolution of the simulation. Simulation results from the continuum gyrokinetic codes GYRO,²³ GS2,¹⁴ and GENE¹³ as well as the PIC gyrokinetic code PG3EQ⁷ are compared in Sec. IV. In Sec. V, we present results from a parameter scan in which the electron heat transport due to ETG turbulence increases from about 3 electron gyro-Bohms to 14 electron gyro-Bohms as the magnetic shear is varied from 0.1 to 0.8. In Sec. VI, we revisit selected analyses of electron heat transport in tokamak discharges, concluding that an electron thermal conductivity between 5 and 10 electron gyro-Bohms is sufficient to explain the electron heat transport in many tokamak discharges. These results are discussed further in Sec. VII.

II. THE BENCHMARK OPERATING POINT

The establishment of a common benchmark is an important step in computational studies of a new regime of plasma microturbulence. This benchmark serves as a means of verifying that different plasma microturbulence simulations codes obtain substantially the same transport and turbulent fluctuation characteristics at a common operating point. The demonstration that a particular plasma microturbulence code can reproduce the benchmark results becomes an important verification exercise for that code. It provides an anchor for future parameter scans, serves to enhance community confidence in the simulation results, and largely eliminates numerical issues when comparing simulation results between codes at different operating points, thereby shifting the focus of discussions from the accuracy of particular simulation codes to the underlying physics issues.

Such a common benchmark was established for ITG turbulence by the Cyclone project.⁸ This effort largely eliminated controversy between practitioners using continuum and particle-in-cell techniques over turbulence simulation results in the ITG regime, and provided a basis for understanding the size scaling of ITG turbulence²⁴ observed in global simulations.^{25,26} Differences between gyrofluid and gyrokinetic simulation results at this benchmark point served to focus attention on the importance of zonal flows generated by ITG turbulence and motivated further development of the theory of zonal flow generation.²⁷⁻²⁹ The numerical models employed in the benchmarking exercise described in this paper differ from those employed for the kinetic simulations of ITG turbulence in Ref. 8 in that the kinetic species is understood to be electrons (rather than ions as in Ref. 8) and the density of the adiabatic species entering the gyrokinetic Poisson equation is proportional to the full potential, ϕ , rather than to the difference between the local potential and its flux surface average, $\phi - \langle \phi \rangle$, as in ITG turbulence simulations. This difference arises because the ions are assumed to have gyro orbits large compared to the perpendicular (to \mathbf{B}) scale of both the ETG modes and any zonal or geodesics acoustic modes generated by the ETG turbulence. We note that previous work^{13,30} shows that finite-ion-orbit effects can be im-

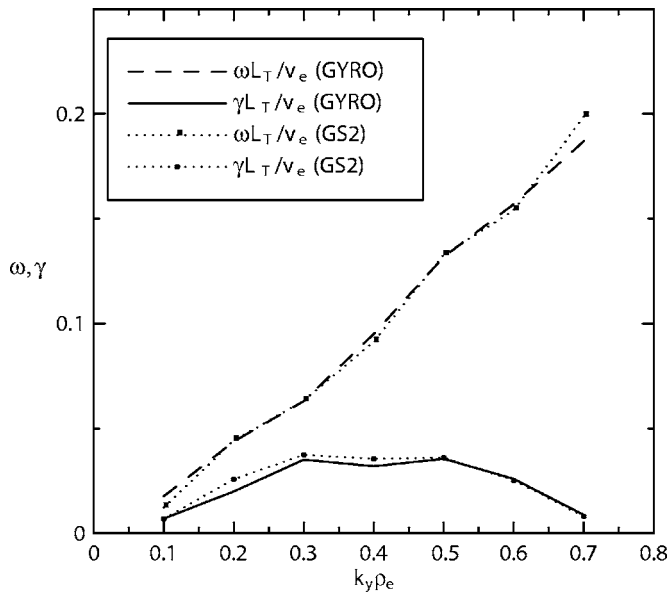


FIG. 1. Linear dispersion relation of ETG modes at the benchmark operating point vs $k_y \rho_e$ as computed by GYRO and GS2 for linear eigenmodes with ballooning mode angle $\theta_0=0$.

portant to the development of the long-wavelength end of the ETG turbulent spectrum, and consider this effect in Sec. V below.

Previous workers^{11,12,19–21,31} have focused on an electron analogue of the operating point chosen for the Cyclone ion temperature gradient benchmark exercise.⁸ This operating point has not produced a successful ETG benchmark. The basic problem is that ETG turbulence is too violent at this operating point, yielding poor performance from all codes. Jenko and Dorland^{13–15} solved this problem in their pioneering work on ETG turbulence simulation by removing the trapped electrons. They accomplished this by reducing the local aspect ratio from the Cyclone benchmark value $r/R=0.18$ to $r/R=0$ where they report $\chi_e \approx 13 (\rho_e/L_T)\rho_e v_{te}$.

Following Jenko and Dorland, we seek an operating point for this ETG benchmarking exercise at which the strength of the ETG turbulence is moderate while retaining the full physics of toroidal plasmas (e.g., trapped particles). Jenko and Dorland¹³ report that the heat transport due to ETG turbulence drops substantially as the magnetic shear is reduced. This motivated our benchmarking exercise at an operating point defined by $R_0/L_T=6.9$, $R_0/L_n=2.2$, $T_e/T_i=1.0$, $q=1.4$, and $s=0.1$. The simulations are performed with kinetic electrons including only electrostatic fields. Motivated by the large ion gyroradius compared to the expected perpendicular scale of ETG turbulence, we take the ion response to be adiabatic both within and across flux surfaces (that is, $\delta n_i/n_0=-q_i\phi/T$). The simulations are performed in flux-tube geometry with a circular plasma cross section and constant magnetic curvature. As discussed in Sec. III, the gyrokinetic code results for this operating point are well converged in all numerical parameters except the perpendicular flux-tube cross section and grid resolution. Hence, efforts to reproduce the ETG benchmark reported here should be performed with flux-tube cross section $L_x=100\rho_e$ and $L_y=64\rho_e$, and should employ a radial grid spacing $\Delta x \leq 2\rho_e$ and sufficient resolution in the binormal (y) direction to resolve fluctuations out to $k_y \rho_e=0.7$. We find that χ_e increases with both flux-tube cross section and spatial resolution in the binormal (y) direction.

These parameters differ from those employed in the Cyclone ITG benchmarking exercise⁸ only in that the magnetic shear, s , has been reduced from 0.79 to 0.1. While this reduction in the magnetic shear produces only a minor change in the linear growth spectrum (the maximum linear growth rate decreases from $\gamma_{\max} \approx 0.04v_{te}/L_T$ at $s=0.79$ to $\gamma_{\max} \approx 0.037v_{te}/L_T$ at $s=0.1$), the heat transport produced by the resulting ETG turbulence drops by about two orders of magnitude. The linear dispersion relation at this operating point is shown in Fig. 1

The linear growth rate for the ETG modes decreases

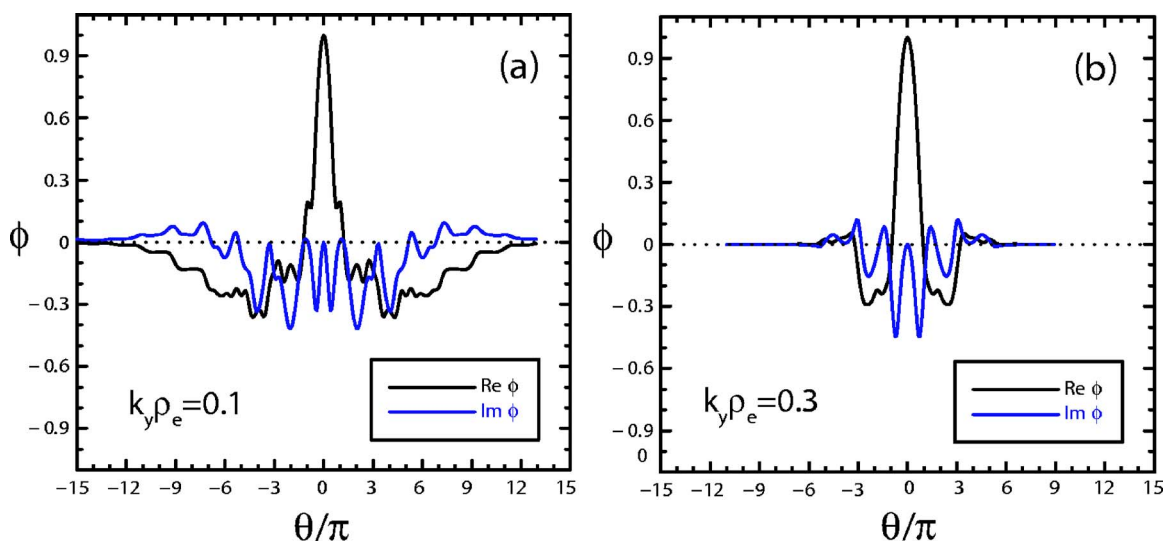


FIG. 2. (Color online) The linear eigenfunctions from GYRO are plotted vs θ for $\theta_0=0$ and (a) $k_y \rho_e=0.1$ and (b) $k_y \rho_e=0.3$. In both cases the real part is shown in black and the imaginary part is shown in blue. The eigenfunctions are normalized to equal 1.0 at $\theta=0$.

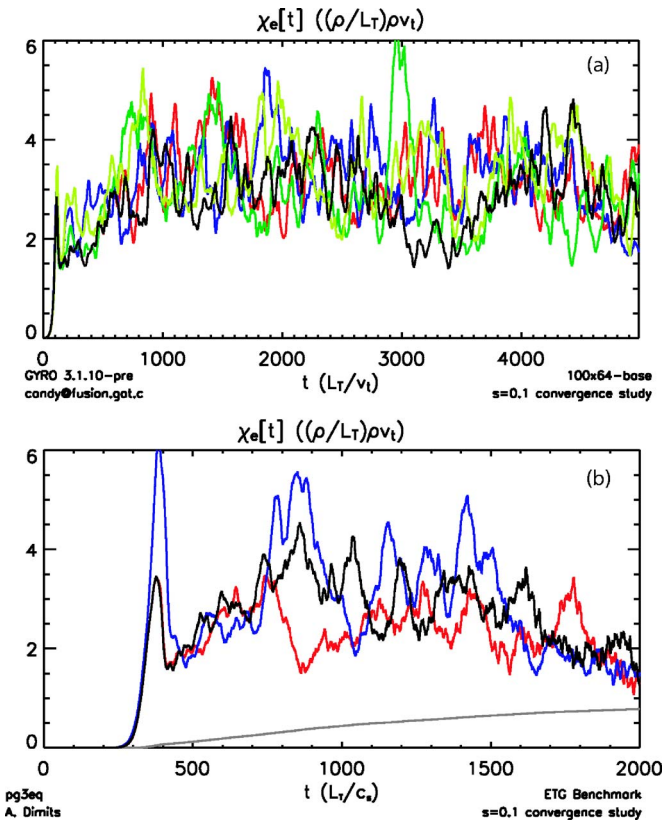


FIG. 3. (Color online) (a) Convergence study at the benchmark point from the GYRO code and (b) from the PG3EQ code. The black curves are the reference simulation. The time step is reduced by 1/2 for the red curve. The velocity space resolution is increased in the blue curves (from 128 to 288 velocity classes for GYRO; and from 16 to 32 particles/cell in PG3EQ). The green curve in (a) shows the effect of decreasing the radial grid spacing from $dr \approx 2\rho_e$ to $dr \approx 1.5\rho_e$ in GYRO, while the chartreuse curve shows the effect of increasing the poloidal resolution. The gray curve in (b) shows the contribution of the discrete particle noise to the total heat transport in the PG3EQ simulation (Ref. 21).

with increasing ballooning mode angle θ_0 , or, equivalently, with increasing midplane radial wave number, $k_{r0}\rho_e = sk_y\rho_e\theta_0$. However, this is quite a weak effect, resulting in a decrease in the growth rate of less than 10% over the full range of ballooning mode angle ($-\pi \leq \theta_0 \leq \pi$) due to the low value of magnetic shear at our benchmark operating point.

The linear eigenmodes for the benchmark operating point are shown in Fig. 2(a) and 2(b). The structure of these eigenmodes on the interval $-\pi \leq \theta \leq \pi$ is only weakly dependent on $k_y\rho_e$. In each case the full width at half-maximum of the eigenfunction in poloidal angle is about π radians. However, the rate at which the eigenfunction falls off at larger values of θ decreases with decreasing $k_y\rho_e$.

III. CONVERGENCE STUDIES

Convergence studies reveal any dependency of the simulation results on the numerical parameters determining the resolution in time, configuration space, velocity space, and dimensions of the simulation volume. Convergence tests with the GYRO code were performed by varying specific parameters about a reference simulation at the benchmark operating point described in Sec. II above. The time step in

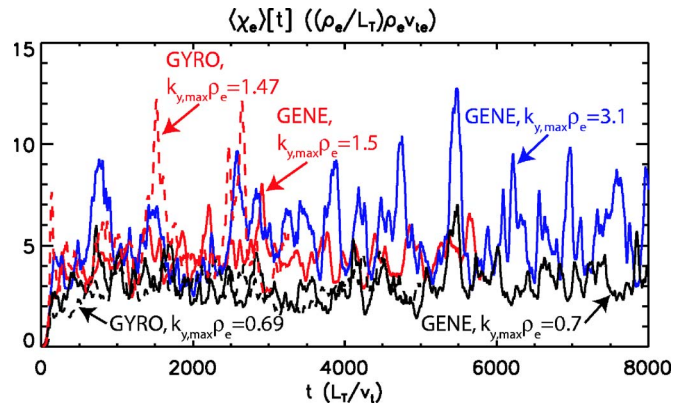


FIG. 4. (Color online) Convergence at the benchmark point in perpendicular grid resolution is investigated by comparing GENE simulations in an $L_x=100\rho_e$ by $L_y=62.82\rho_e$ flux tube with eight binormal modes such that $k_{y,max}\rho_e=0.7$ (black curve), 16 k_y modes such that $k_{y,max}\rho_e=1.5$ (red curve), and 32 k_y modes such that $k_{y,max}\rho_e=3.1$ (blue curve). Gyro simulations with 8 k_y modes such that $k_{y,max}\rho_e=0.69$ (dashed black curve) and 16 k_y modes such that $k_{y,max}\rho_e=1.47$ (dashed red curve) are shown for comparison.

the reference GYRO simulation is $dt=0.025 a/v_{te} \approx 0.063L_T/v_{te}$. The k -space resolution is determined by the flux-tube cross section $L_x=101.86\rho_e$ and $L_y=64\rho_e$. There are 50 radial grid points providing a grid resolution of $\Delta r \approx 2\rho_e$. GYRO employs a Fourier representation in toroidal angle, retaining eight Fourier modes in the base-case simulations, which provides resolution out to $k_{\perp}\rho_e \approx 0.69$ at the outboard midplane. Velocity space is represented using a grid with eight energies, eight angles (four trapped and four passing), and two signs of the parallel velocity for a total of 128 velocity classes at each spatial grid point. The reference case for the PG3EQ simulations employs a time step $dt=0.05L_T/v_{te}$ and a flux-tube cross section $L_x=101.86\rho_e$ by $L_y=64\rho_e$. The grid spacing is $dx=0.795775\rho_e$ by $dy=\rho_e$. Variations along B are represented with 32 grid points. Velocity space is sampled with 16 particles/grid cell.

Figure 3 shows the results of convergence tests about the reference operating point. Demonstrating well-converged re-

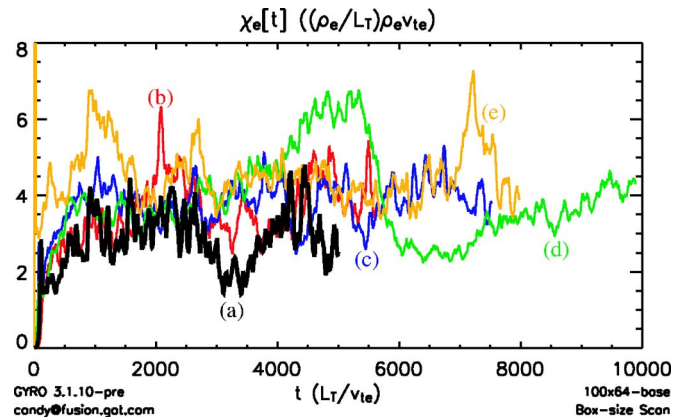


FIG. 5. (Color online) The electron thermal conductivity, $\chi_e(t)$, from a sequence of GYRO simulations in which the flux-tube cross section, $L_x \times L_y$, varies from (a) $100\rho_e \times 64\rho_e$ (black curve), through (b) $128\rho_e \times 128\rho_e$ (red curve) and (c) $256\rho_e \times 128\rho_e$ (blue curve) to (d) $256\rho_e \times 256\rho_e$ (green curve). (e) The simulation at $256\rho_e \times 128\rho_e$ is repeated using kinetic (instead of adiabatic) ions (gold curve).

TABLE I. Convergence in binormal resolution.

Code/resolution	$k_{x,\max}\rho_e$	$k_{y,\max}\rho_e$	$\langle\chi_e\rangle$
1) GENE, reference	2.0	0.70	$2.95\pm 0.15 (\rho_e/L_T)\rho_e v_{te}$
2) GYRO, reference	~ 0.79	0.69	$2.94\pm 0.11 (\rho_e/L_T)\rho_e v_{te}$
3) GENE, intermediate	4.0	1.50	$5.13\pm 0.30 (\rho_e/L_T)\rho_e v_{te}$
4) GYRO, intermediate	~ 1.57	1.47	$5.41\pm 0.16 (\rho_e/L_T)\rho_e v_{te}$
5) GENE, high resolution	2.0	3.10	$5.48\pm 0.18 (\rho_e/L_T)\rho_e v_{te}$
6) GENE, high resolution	3.0	3.10	$5.66\pm 0.23 (\rho_e/L_T)\rho_e v_{te}$

Note: The average of $\chi_e(t)$ over the interval from $t=1000 L_T/v_{te}$ to the end of the run for GENE and GYRO simulations used in the bi-normal resolution convergence study. The radial resolution for GYRO, which employs finite difference techniques in the radial dimension, is estimated as $k_{x,\max}\rho_e \approx \pi/(2\Delta x)$.

sults from a single code provides a sufficient basis for this benchmarking exercise. However, given the controversy over ETG simulation results from continuum and PIC codes, we have chosen to present convergence studies from both the continuum code GYRO and the PIC code PG3EQ. These convergence tests examine variations in $\chi_e \equiv -Q_e/n_0 \nabla T_0$ (where Q_e is the volume-averaged electron heat flux while n_0 and ∇T_0 are the equilibrium density and the equilibrium temperature gradient) as numerical parameters of these simulations are varied. We conclude from Fig. 3 that both the GYRO and PG3EQ codes are converged in time step (this is not an issue for the GENE and GS2 codes as they have automatic time-step control) and velocity-space resolution. In addition, GYRO is converged in spatial resolution in both the radial and poloidal (along the field-line) directions.

Convergence with grid spacing in the binormal direction (i.e., the direction within the flux surface perpendicular to \mathbf{B}) is more problematic. We investigated this issue by comparing GYRO and GENE simulations in which the spatial resolution in the binormal is increased by increasing the number of Fourier modes at fixed flux-tube cross section from eight Fourier modes for a binormal resolution of $k_{y,\max}\rho_e=0.7$ (the reference case employed above), to 16 Fourier modes ($k_{y,\max}\rho_e=1.5$), and finally 32 Fourier modes ($k_{y,\max}\rho_e=3.1$) in the binormal (see Fig. 4). The GENE simulations represented variations along \mathbf{B} with 16 grid points, while velocity space is represented with 32 parallel velocities and 8 magnetic moments, for a total of 256 velocity classes at each spatial grid point. The flux-tube cross section in these GENE simulations was $L_x=100\rho_e$ by $L_y=62.82\rho_e$.

We find that our reference case with eight Fourier modes in the binormal is not converged in binormal resolution (see Table I). Averaging χ_e over $t > 1000 L_T/v_{te}$, the eight-mode GENE and GYRO simulations are in agreement with $\langle\chi_e\rangle \approx 2.95(\rho_e/L_T)\rho_e v_{te}$ (GENE, $k_{y,\max}\rho_e=0.7$) and $\langle\chi_e\rangle \approx 2.94(\rho_e/L_T)\rho_e v_{te}$ (GYRO, $k_{y,\max}\rho_e=0.69$). When the resolution in the binormal direction is doubled (so that the maximum binormal wave number resolved increases from $k_{y,\max}\rho_e \approx 0.7$ to $k_{y,\max}\rho_e \approx 1.5$) we find that $\langle\chi_e\rangle$ increases by 74%. The GENE and GYRO simulation codes agree on the magnitude of the electron heat transport in this intermediate resolution case, with GENE finding $\langle\chi_e\rangle \approx 5.13(\rho_e/L_T)\rho_e v_{te}$ (see line 3 of Table I and GYRO finding $\langle\chi_e\rangle \approx 5.41(\rho_e/L_T)\rho_e v_{te}$ (see line 4 of Table I). Comparing this intermediate resolution GENE simulation (which em-

ployed 16 Fourier modes in the binormal and resolved out to $k_{y,\max}\rho_e=1.5$) to the high resolution GENE simulation (which employed 32 Fourier modes and resolved out to $k_{y,\max}\rho_e \approx 3.10$) we find that $\langle\chi_e\rangle$ increases only another 10% to $\langle\chi_e\rangle \approx 5.66(\rho_e/L_T)\rho_e v_{te}$ —less than the sum of the error bars on our estimates of $\langle\chi_e\rangle$ (compare lines 3 and 6 of Table I). We conclude that convergence in binormal resolution is achieved with 16 or more Fourier modes. That is, binormal resolution to $k_{y,\max}\rho_e > 1.4$ is required for convergence. Taking the time interval weighted average of $\langle\chi_e\rangle$ from all simulations with $k_{y,\max}\rho_e > 1.4$ we estimate the converged value of the electron heat flux in a $100\rho_e \times 64\rho_e$ flux tube as $\langle\chi_e\rangle = 5.45 \pm 0.19(\rho_e/L_T)\rho_e v_{te}$.

The radial resolution was varied along with the binormal resolution in this binormal resolution convergence study. Varying the radial grid resolution at the highest binormal resolution, we find that $\langle\chi_e\rangle$ is insensitive to the radial resolution for $k_{x,\max}\rho_e > 1.5$, (see lines 4 through 6 of Table I).

We investigate convergence with respect to flux tube cross section at a binormal resolution of $k_{y,\max}\rho_e=0.69$. Simulations at this reference operating point are reasonably well converged in flux-tube cross section. Figure 5 shows a sequence of four GYRO simulations in which the flux-tube cross section is increased from ($L_x=100\rho_e, L_y=64\rho_e$) to ($L_x=256\rho_e, L_y=256\rho_e$).

We see that $\langle\chi_e\rangle$ increases slowly with increasing flux-tube cross section. The time averages of $\chi_e(t)$ over the interval $t > 1000 L_T/v_{te}$ are presented in Table II. The dependence of $\langle\chi_e\rangle$ on the binormal dimension of the flux tube, L_y , is reasonably well fit by $\langle\chi_e\rangle \approx 2.77 + 0.0074^* L_y/\rho_e$, where $\langle\chi_e\rangle$ is in units of $(\rho_e/L_T)\rho_e v_{te}$. A comparison between runs (b) $128\rho_e \times 128\rho_e$ and (c) $256\rho_e \times 128\rho_e$ reveals little depen-

TABLE II. $\langle\chi_e\rangle$ vs flux-tube cross section.

Flux-tube cross section	L_x	L_y	χ_e
(a) $100\rho_e \times 64\rho_e$, adiabatic ions	$100\rho_e$	$64\rho_e$	$2.94\pm 0.11 (\rho_e/L_T)\rho_e v_{te}$
(b) $128\rho_e \times 128\rho_e$, adiabatic ions	$128\rho_e$	$128\rho_e$	$3.76\pm 0.08 (\rho_e/L_T)\rho_e v_{te}$
(c) $256\rho_e \times 128\rho_e$, adiabatic ions	$256\rho_e$	$128\rho_e$	$3.86\pm 0.07 (\rho_e/L_T)\rho_e v_{te}$
(d) $256\rho_e \times 256\rho_e$, adiabatic ions	$256\rho_e$	$256\rho_e$	$4.51\pm 0.11 (\rho_e/L_T)\rho_e v_{te}$
(e) $256\rho_e \times 128\rho_e$, kinetic ions	$256\rho_e$	$128\rho_e$	$3.96\pm 0.24 (\rho_e/L_T)\rho_e v_{te}$

Note: The average of $\chi_e(t)$ over the interval from $t=1000v_{te}/L_T$ to the end of the simulation for the flux-tube cross-section scan shown in Fig. 5.

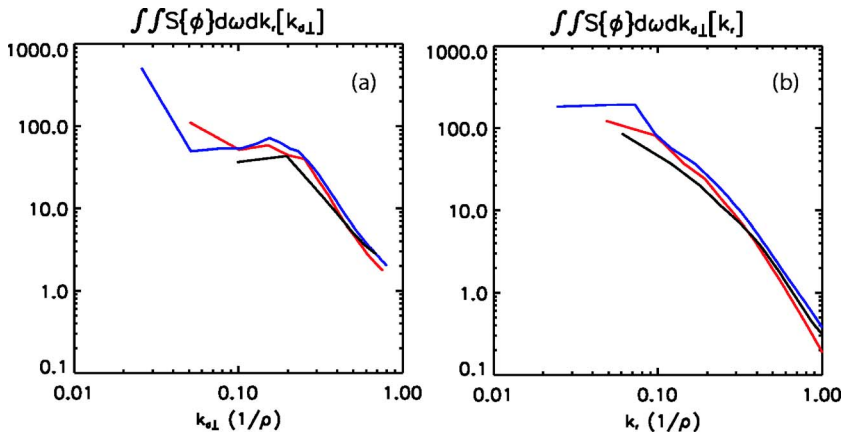


FIG. 6. (Color online) Fluctuation spectrum of the electrostatic potential at the outboard midplane is plotted (a) vs the wave number in the binormal direction and (b) vs wave number in the radial direction for GYRO runs with flux-tube cross section $L_x=100\rho_e$ by $L_y=64\rho_e$ (black curve), $L_x=128\rho_e$ by $L_y=128\rho_e$ (red curve), and $L_x=256\rho_e$ by $L_y=256\rho_e$ (blue curve).

dence of $\langle\chi_e\rangle$ on the radial dimension of the flux tube, L_x ; while a comparison between runs (c) $256\rho_e \times 128\rho_e$ (adiabatic ions) and (e) $256\rho_e \times 128\rho_e$ (kinetic ions) reveals that replacing adiabatic ions with kinetic ions (using a mass ratio of $m_i/m_e=400$) makes very little difference in $\langle\chi_e\rangle$.

The tendency for χ_e to increase with binormal extent of the simulation, L_y , leads us to examine the fluctuation spectrum in an effort to understand why box-size convergence is proving elusive. Figure 6 shows that the fluctuation spectrum converges with increasing L_y at large $|k|$ ($|k\rho_e|>0.2$), where it falls off as $|\phi(k)|^2 \sim 1/k^2$. Figure 6(a) shows that below $k_y\rho_e \approx 0.2$ the k_y spectrum fails to converge with the box size because the intensity increases at low k_y as the box size is increased. In contrast, Fig. 6(b) shows that the k_r spectrum is well-behaved at small $k_r\rho_e$. The divergence of the k_y spectrum as $k_y\rho_e \rightarrow 0$ explains the lack of convergence with increasing L_y , while the absence of this divergence in the k_r spectrum allows convergence as L_x is increased.

This same information can be cast in terms of the correlation function. Figure 7(a) shows the correlation function versus the binormal separation, while Fig. 7(b) shows the correlation function versus the radial separation. The correlation function is well-converged for $L_x \geq 125\rho_e$ at separations less than about $10\rho_e$ (corresponding to large k_\perp) in both binormal and radial directions. However, the fall off at large separation decreases as the flux-tube cross section is

increased, reflecting the presence of significant fluctuation intensity in long-wavelength modes.

The convergence in flux-tube cross section would be improved if the benchmark operating point were modified such that there was a long-wavelength cutoff in the fluctuation spectrum. This might be accomplished within the adiabatic ion/kinetic electron model employed here by choosing a more realistic magnetic geometry with good average curvature (the flux-surface average curvature for the magnetic geometry considered here is exactly zero), or by including electromagnetic fields in the expectation that they may provide a long-wavelength cutoff at $k_y c/\omega_{pe} \approx 1$. More generally, it has already been demonstrated that replacing the adiabatic ion model with kinetic ions provides the long-wavelength dynamics required to achieve proper box-size convergence.^{13,30}

IV. CROSS-CODE COMPARISONS

Having demonstrated that our gyrokinetic simulation codes are well-behaved at the chosen operating point, we now turn to cross-code comparisons. Gyrokinetic simulations of ETG turbulence have been performed at the benchmark point described in Sec. II with the continuum gyrokinetic codes GYRO,²³ GS2,¹⁴ and GENE,¹³ and the particle-in-cell code PG3EQ.⁷ The electron thermal conductivity results,

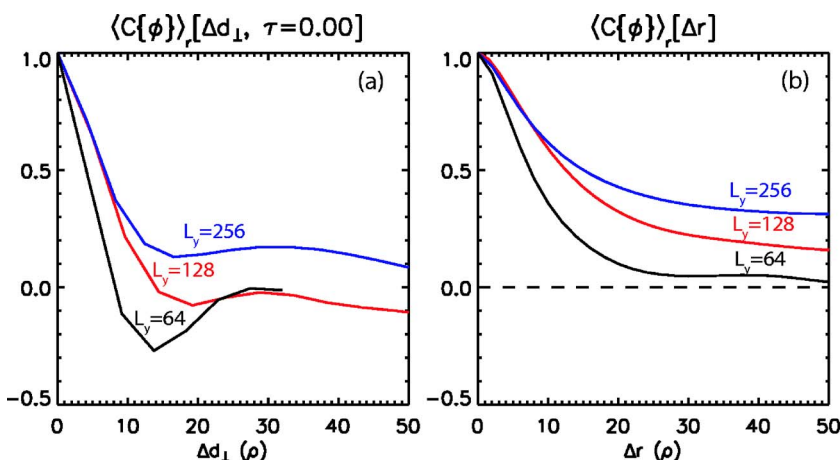


FIG. 7. (Color online) The correlation function of the midplane potential is plotted (a) vs. separation in the binormal direction and (b) vs separation in the radial direction for GYRO simulations with flux-tube cross sections of $L_x=100\rho_e$ by $L_y=64\rho_e$ (black curve), $L_x=128\rho_e$ by $L_y=128\rho_e$ (red curve), and $L_x=256\rho_e$ by $L_y=256\rho_e$ (blue curve).

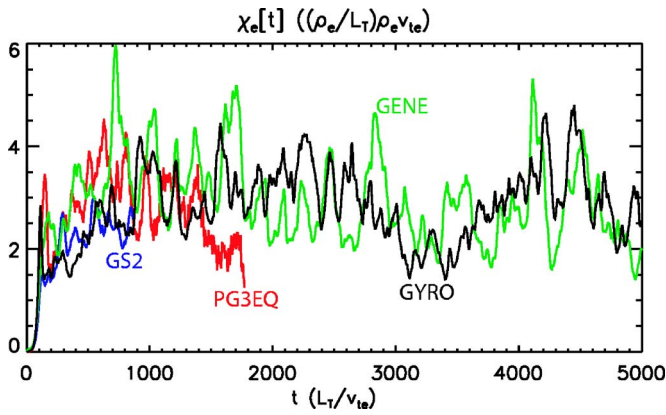


FIG. 8. (Color online) $\chi_e \equiv -Q_e/n_0 \nabla T_0$, from GYRO (black curve), GS2 (blue curve), GENE (green curve), and PG3EQ (red curve) are plotted vs time.

$\chi_e \equiv -Q_e/n_0 \nabla T_0$, from GYRO, GS2, GENE, and PG3EQ are plotted versus time in Fig 8.

The numerical resolution in GYRO, PG3EQ, and GENE is as described for the reference case in Sec. III above. The GS2 code adjusts its time step to insure accuracy of the time integration. It was run with a flux-tube cross section of $L_x = 101.8\rho_e$ and $L_y = 64\rho_e$. GS2 employs a Fourier representation in the plane perpendicular to \mathbf{B} with 21 radial modes, 11 modes in the binormal, and 30 grid points along \mathbf{B} . Velocity space was represented with 8 energies by 36 angles and two signs of the parallel velocity for a total of 576 velocity classes at each spatial grid point.

Averaging $\chi_e(t)$ over the maximum interval of steady-state turbulence in each code ($500 < t < 5000$ for GYRO; $300 < t < 873$ for GS2; $500 < t < 10000$ for GENE; and $500 < t < 2000$ for PG3EQ), we find $\langle \chi_e \rangle_{\text{GYRO}} = 2.93$ ($\rho_e/L_T \rho_e v_{te}$), $\langle \chi_e \rangle_{\text{GS2}} = 2.38$ ($\rho_e/L_T \rho_e v_{te}$), $\langle \chi_e \rangle_{\text{GENE}} = 2.98$ ($\rho_e/L_T \rho_e v_{te}$), and $\langle \chi_e \rangle_{\text{PG3EQ}} = 2.85$ ($\rho_e/L_T \rho_e v_{te}$), for a (time-interval) weighted average and standard deviation of $\langle \chi_e \rangle = 2.93 \pm 0.11$ ($\rho_e/L_T \rho_e v_{te}$). The time-interval weighted standard deviation in $\langle \chi_e \rangle$ between codes yields an error in our estimate of the mean of less than 10%. This agreement between codes is better than that achieved in the Cyclone ITG benchmarking exercise.⁸

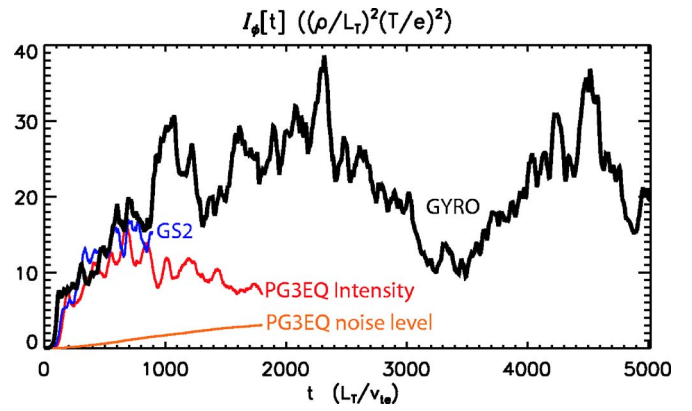


FIG. 9. (Color online) The fluctuation intensity, $\langle \delta\phi^2 \rangle$, averaged over the outboard midplane from GYRO (black curve), GS2 (blue curve), and PG3EQ (red curve). The contribution of discrete particle noise to the PG3EQ fluctuation intensity is shown by the orange curve.

The electron thermal transport is the quantity of greatest macroscopic interest. However, a detailed code benchmarking also requires a comparison of the microscopic fluctuations. These fluctuations can be characterized by the fluctuation intensity averaged over the outboard midplane, $\langle \delta\phi^2 \rangle$, the two-point correlation function of $\delta\phi$,

$$C\{\delta\phi\} \equiv \frac{\langle \delta\phi(\vec{x} + \Delta, t - \tau) \delta\phi(\vec{x}, t) \rangle}{\langle \delta\phi(\vec{x}, t)^2 \rangle}, \quad (1)$$

and the spectral density,

$$S\{\delta\phi\} \equiv \langle |\delta\phi(k, \omega)|^2 \rangle. \quad (2)$$

The ETG fluctuations are isolated from the $n=0$ modes (zonal flows and geodesic-acoustic modes which do not produce any radial transport) by defining $\delta\phi$ to be the deviation of the midplane potential from its toroidal average.

Figure 9 displays the ETG fluctuation intensities from GYRO, GS2, and PG3EQ. The late-time ($t > 900L_T/v_{te}$) drop in the ETG fluctuation intensity from PG3EQ is probably due to the accumulation of discrete particle noise.²¹ We see that the intensity of the ETG turbulent fluctuations from each of these codes is substantially the same.

Figures 10(a) and 10(b) display estimates of $C\{\delta\phi\}$ from

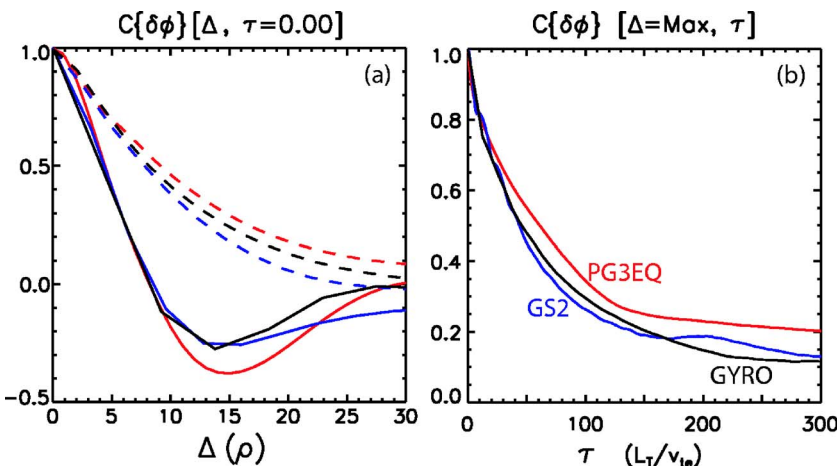


FIG. 10. (Color online) (a) The two-point correlation function from GYRO (black curves), GS2 (blue curves), and PG3EQ (red curves) is displayed as a function of the binormal separation (solid curves) and the radial separation (dashed curves) at $\tau=0$. (b) The two-point correlation function is displayed as a function of the time lag. The spatial separation, Δ , is chosen at each value of τ so as to maximize $C\{\delta\phi\}$.

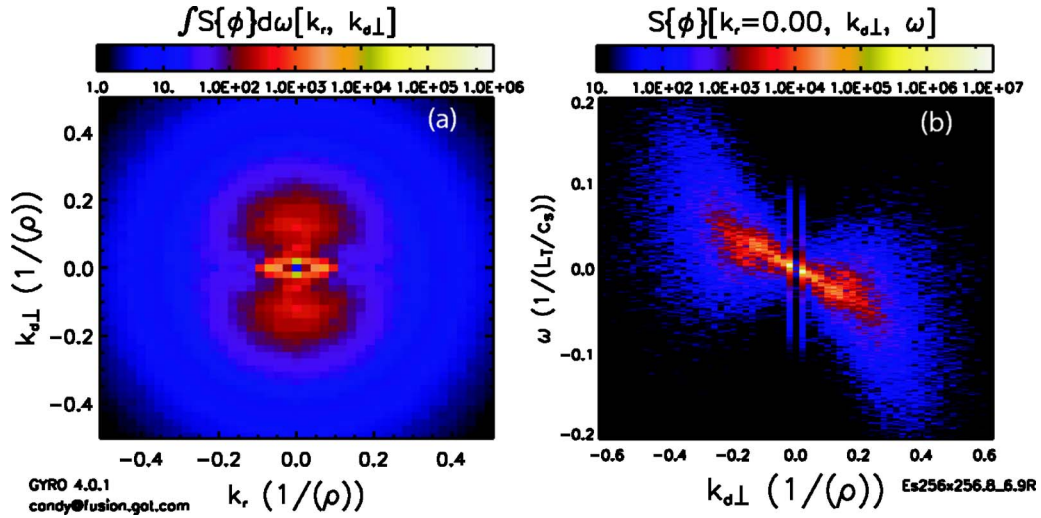


FIG. 11. (Color online) Spectral density of electrostatic potential fluctuations at the $s=0.1$ benchmark point (a) vs (k_r, k_\perp) and (b) vs (k_\perp, ω) .

the GYRO, PG3EQ, and GS2 benchmark runs as a function of both the spatial separation, Δ , and the time lag, τ . These estimates of the correlation function are seen to be in substantial agreement. Defining the radial correlation length, ℓ_r , as the full width at half-maximum of the correlation function versus the radial separation, we find $\ell_r \approx 17.5 \pm 1.0 \rho_e$. Similarly, the transverse eddy width, ℓ_\perp , is defined as the full width at half-maximum of the correlation function versus the binormal separation. We find $\ell_\perp \approx 9.1 \pm 1.01 \rho_e$. That is, a typical turbulent eddy has a mild radial elongation with an aspect ratio of about 2, similar to previous simulations of ETG turbulence.³² The eddy lifetime, τ_{eddy} , is defined as the full width at half-maximum of the correlation function versus time lag, where the spatial separation is chosen at each value of τ so as to maximize $C\{\delta\phi\}$. This somewhat more complex procedure is chosen because the turbulent eddies propagate (mainly in the binormal direction) and it is our goal to characterize the lifetime of a typical turbulent eddy rather than the time required for a typical turbulent eddy to move past a stationary observer (which would be given by the full width at half-maximum of $C\{\delta\phi\}$ versus τ evaluated at $\Delta=0$). We find $\tau_{\text{eddy}} \approx 100 \pm 10 L_T/v_{te}$.

The fluctuation spectrum in the (k_r, k_\perp) plane is markedly anisotropic at low wave number ($|k\rho_e| < 0.2$), with k_\perp generally larger than k_r . At larger wave number ($|k\rho_e| > 0.2$), the spectrum becomes isotropic in the plane perpendicular to \mathbf{B} [see Fig. 11(a)]. Considered as a function of frequency and binormal wave number, k_\perp , we see that the turbulent fluctuations are generally well-organized at lower k_\perp ($k_\perp \rho_e < 0.2$) in the sense that they have a well-defined frequency as a function of k_\perp , such that $\omega \approx 0.2(\rho_e/L_T)k_\perp v_{te}$. At larger wave numbers ($k_\perp \rho_e > 0.2$), the turbulent fluctuations are disorganized, such that the frequency is no longer well-defined as a function of the wave number [see Fig. 11(b)].

Having demonstrated that ETG turbulence as characterized by the intensity and correlation function of $\delta\phi$ is substantially the same in the benchmark simulations from GYRO, PG3EQ, and GS2, we turn our attention to the

$n=0$ component of the potential, $\langle\phi\rangle(r, t)$. Considerations of gauge and Galilean invariance imply that the $n=0$ component of the potential mainly affects the ETG turbulence and the resulting anomalous transport through the shear in the $n=0$ component of the $E \times B$ flow. Shear in the $E \times B$ flow leads to decorrelation of the turbulent eddies at a rate proportional to the $E \times B$ flow shear.^{33–35} For the ETG simulations in question, there is no externally imposed $E \times B$ flow shear. We can characterize the decorrelation due to the time- and space-dependent flow shear generated by $\langle\phi\rangle(r, t)$ through the shear decorrelation rate,

$$\Gamma_{E \times B} = \left(\frac{\ell_r}{\ell_\perp} \right) \left\langle \left| \frac{\partial}{\partial r} V_{E \times B} \right|^2 \right\rangle^{1/2}, \quad (3)$$

where ℓ_r and ℓ_\perp are the radial and binormal correlation lengths of the ETG turbulence defined above, while $\partial V_{E \times B} / \partial r$ is the shear in the $E \times B$ flow at spatial scales large compared to the radial eddy width, ℓ_r , and at time scales such that the flow pattern persists for times long compared to the eddy lifetime, τ_{eddy} . The rms flow shear, $\langle |\partial V_{E \times B} / \partial r|^2 \rangle^{1/2}$, is computed using digital filters to remove spatial scales shorter than ℓ_r and time scales shorter than τ_{eddy} and displayed in Fig. 12. We find that there is substantial agreement between GYRO, PG3EQ, and GS2 in the rms flow shear, $\langle |\partial V_{E \times B} / \partial r|^2 \rangle^{1/2} \approx 0.027 \pm 0.004 v_{te} / L_T$.

It follows that the shear decorrelation rate, $\Gamma_{E \times B} \approx 0.054 \pm 0.01 v_{te} / L_T$, is comparable to the linear growth rate of the fastest growing mode, $\gamma_{\text{max}} = 0.037 v_{te} / L_T$. This result is similar to that found in gyrokinetic simulations of ETG turbulence in stellarators.³² Values of the background shear decorrelation rate in excess of the maximum linear growth rate can suppress ITG turbulence.^{5,33} Turbulence-driven zonal flows are known to play a key role in ITG turbulence saturation, where the shearing rate of the zonal flows is comparable to the fastest growing linear ITG mode (see, for example, the gyrofluid simulations in Ref. 35). It is interesting to note that both ETG and ITG turbulence appear to exhibit self-regulation such that $\Gamma_{E \times B} \sim \gamma_{\text{max}}$. The ETG simulations

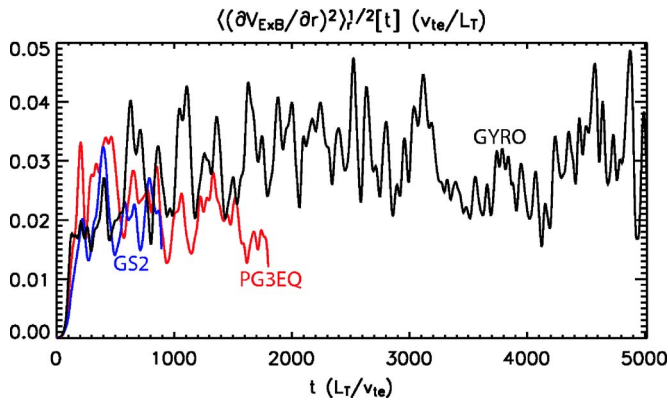


FIG. 12. (Color online) The *rms* flow shear is displayed vs time from GYRO (black curve), PG3EQ (red curve), and GS2 (blue curve).

reach much larger values of $\chi / \chi_{\text{gyroBohm}}$ before achieving this balance because the coupling of ETG modes to zonal flows is weaker than that of ITG modes. At these parameters ITG turbulence produces transport levels (as measured in ion gyro-Bohms) of $\chi_i \approx 0.6(\rho_i / L_T) \rho_i v_{ti}$, which are substantially lower than those obtained here for ETG turbulence [$\chi_e \approx 3(\rho_e / L_T) \rho_e v_{te}$].

V. MAGNETIC SHEAR SCAN

A key issue for ETG turbulence is whether it is capable of producing a large electron heat flux. The electron thermal conductivity must be larger than about 5 $(\rho_e / L_T) \rho_e v_{te}$ to be consistent with transport analysis from tokamak experiments (see Sec. VI). Jenko and Dorland's work¹³ leads us to expect that there will be a substantial increase in the electron thermal transport as the magnetic shear is increased past $s=0.4$. Figure 13 shows the electron thermal conductivity from a sequence of GYRO and GENE simulations in which the magnetic shear is varied at a binormal resolution $k_{y,\text{max}} \rho_e = 0.69$ (these simulations were performed before we discovered that convergence in binormal resolution requires $k_{y,\text{max}} \rho_e > 1.4$). As the magnetic shear is varied over the range $0.1 \leq s \leq 0.35$, the initial transient in the heat flux becomes more dramatic while the late-time ($t > 1500 L_T / v_{te}$ for GYRO simulations and $t > 2500 L_T / v_{te}$ for GENE simulations) average of χ_e remains substantially unchanged, varying between 2.7 and 3.8 $(\rho_e / L_T) \rho_e v_{te}$. When the magnetic shear is increased further to $s=0.4$, the electron thermal conductivity takes a dramatic jump to $\langle \chi_e \rangle \approx 200(\rho_e / L_T) \rho_e v_{te}$ (GYRO) or 73 $(\rho_e / L_T) \rho_e v_{te}$ (GENE).

Substantially similar results are obtained from both GS2 and PG3EQ. In particular, we confirm this dramatic increase in the electron thermal transport at $s=0.4$ by reproducing this simulation with GS2 and PG3EQ as illustrated in Fig. 14 below. These values of χ_e are much larger than those obtained by Jenko and Dorland,¹³⁻¹⁵ who performed simulations without trapped particles obtaining $\chi_e \approx 13 \chi_{e,\text{GB}}$.

When the magnetic shear is increased to $s=0.4$, the spectral density in the (k_r, k_\perp) plane becomes nearly monochromatic, with almost all of the intensity concentrated in a single mode at $k_r \rho_e = 0$, and $k_\perp \rho_e \approx 0.1$ (this is the longest wavelength in the binormal direction allowed by the bound-

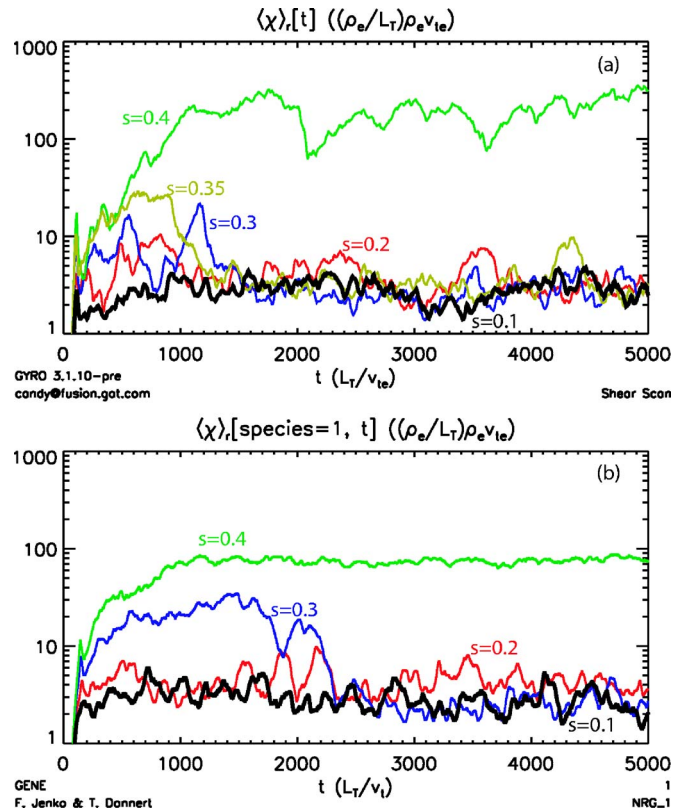


FIG. 13. (Color online) $\chi_e \equiv -Q_e / n_0 \nabla T_0$, from a sequence of simulations with flux-tube cross section of $L_x = 100 \rho_e$ by $L_y = 64 \rho_e$ using (a) GYRO in which the magnetic shear is varied through $s=0.1$ (black curve), $s=0.2$ (red curve), $s=0.3$ (blue curve), $s=0.35$ (olive curve), and $s=0.4$ (green curve); and (b) GENE in which the magnetic shear is varied through $s=0.1$ (black curve), $s=0.2$ (red curve), $s=0.3$ (blue curve), and $s=0.4$ (green curve).

ary conditions). Considered as a function of frequency and binormal wave number, k_\perp , the fluctuations are again well-organized at lower k_\perp ($k_\perp \rho_e < 0.2$) and disorganized at larger wave numbers ($k_\perp \rho_e > 0.2$).

The transition to a nearly monochromatic spectrum occurs abruptly as the magnetic shear is increased and is closely associated with the sharp increase in the electron heat transport as the magnetic shear is increased from $s=0.3$ to

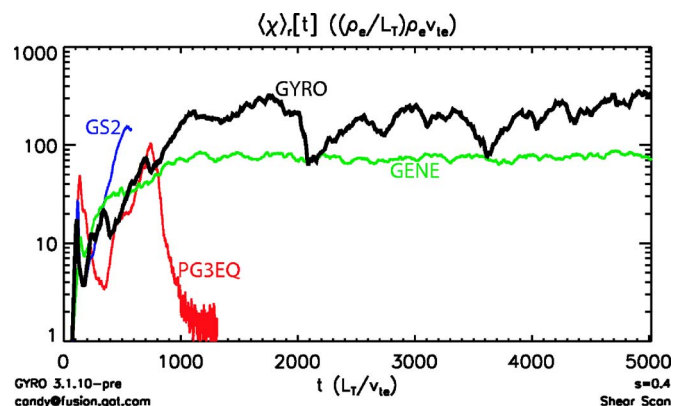


FIG. 14. (Color online) $\chi_e \equiv -Q_e / n_0 \nabla T_0$ at $s=0.4$ from GYRO (black curve), GS2 (blue curve), GENE (green curve), and PG3EQ (red curve). The late-time ($t > 750 L_T / v_{te}$) drop in χ_e from PG3EQ is due to the accumulation of discrete particle noise (Ref. 21).

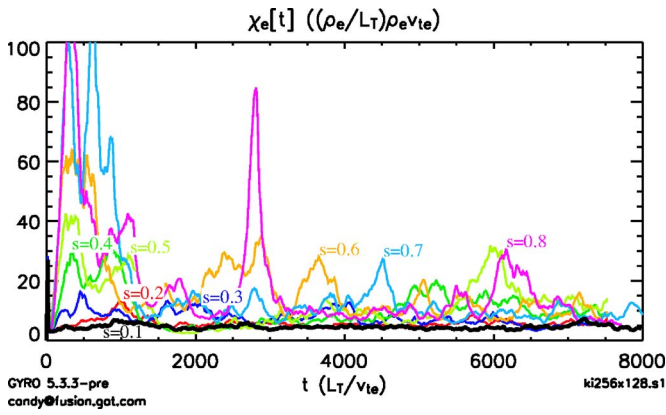


FIG. 15. (Color online) The electron thermal transport from a GYRO magnetic shear scan with kinetic ions, including $s=0.1$ (black curve), $s=0.2$ (red curve), $s=0.3$ (blue curve), $s=0.4$ (green curve), $s=0.5$ (chartreuse curve), $s=0.6$ (gold curve), $s=0.7$ (turquoise curve), and $s=0.8$ (purple curve).

0.4. Very high electron heat transport [$\chi_e \gg 10(\rho_e/L_T)\rho_e v_{te}$] is, in our experience, always accompanied by a nearly monochromatic fluctuation spectrum with $k_r \approx 0$. This spectrum corresponds to coherent “streamers” with a macroscopic radial scale in the perpendicular plane within configuration space.

This rapid increase in the electron heat transport with increasing shear would appear to be the most dramatic result of our study of ETG turbulence. As such, we employed the GYRO code to repeat the magnetic shear scan with the adiabatic ions replaced by full gyrokinetic ions at a mass ratio of $m_i/m_e=400$. Figure 15 shows $\chi_e(t)$ from these simulations, which employed a somewhat larger flux-tube cross section, $256\rho_e \times 128\rho_e$, and binormal resolution $k_{y,max}\rho_e=0.69$.

With kinetic ions the intensity of the initial burst of turbulence increases with increasing magnetic shear (as was the case for adiabatic ions, see Fig. 13 above). However, the electron heat flux drops back down so that the late-time average remains modest (see Table III).

Comparing this magnetic shear scan with kinetic ions to a similar scan with adiabatic ions and the same flux-tube dimensions and grid resolution, we find that the adiabatic ion model breaks down when the magnetic shear exceeds $s=0.4$. Instead of the dramatic increase of $\langle\chi_e\rangle$ with increasing magnetic shear found with the adiabatic ion model, simula-

tions with gyrokinetic ions show a modest, but steady increase in $\langle\chi_e\rangle$ with increasing magnetic shear over the interval $0.1 \leq s \leq 0.6$.

These simulations were not converged in binormal resolution (they were performed before we uncovered this problem). We anticipate that a magnetic shear scan at higher binormal resolution would show a similar trend with $\langle\chi_e\rangle$ increasing with increasing magnetic shear, while the overall magnitude of $\langle\chi_e\rangle$ may be as much as a factor of 2 higher consistent with the 90% increase in $\langle\chi_e\rangle$ observed in our binormal convergence study at $s=0.1$. On the other hand, ETG transport may be reduced in the presence of long-wavelength ITG/TEM (trapped electron mode) turbulence. The interaction of ETG and ITG/TEM is currently under study and is being reported on elsewhere.³¹

VI. ELECTRON TRANSPORT RATES IN EXPERIMENT

Transport analyses of DIII-D,³⁶ JET,³⁷ and JT-60U³⁸ discharges suggest that ETG turbulence may be responsible for the electron heat transport across thermal barriers, in the L-mode edge of discharges with internal transport barriers, and in the outer half of H-mode discharges.³⁹ For example, scaling experiments on the DIII-D tokamak³⁹ show that electron and ion heat transport in the outer half of H-mode discharges have different scaling with $\rho^* = \rho/a$, indicating that there is a fundamental difference in the mechanisms responsible for the electron and ion heat transport in these discharges. In this region, the electron heat transport is unaffected by changes in the $E \times B$ shearing rate and exhibits nearly gyro-Bohm scaling with ρ^* as one would expect if the electron heat transport resulted from ETG turbulence. However, the near isomorphism between ITG and ETG turbulence involves exchanging ion scales (the ion gyroradius, ρ_i , and the ion thermal velocity, v_{ti}) for the corresponding electron scales (the electron gyroradius, ρ_e , and the electron thermal velocity, v_{te}). As a result, the transport associated with ETG turbulence is measured in electron gyro-Bohms. In deuterium plasmas, electron gyro-Bohms are 60 times smaller than the ion gyro-Bohms used to calibrate the ITG turbulence thought to be responsible for much of the energy transport observed in tokamak experiments. This factor of 60 has led to great skepticism regarding the practical significance of ETG turbulence to electron transport in tokamak experi-

TABLE III. $\langle\chi_e\rangle$ vs magnetic shear.

	$s=0.1$	$s=0.2$	$s=0.3$	$s=0.4$	$s=0.5$	$s=0.6$	$s=0.7$	$s=0.8$
Adiabatic ions	3.9 ± 0.1	5.3 ± 0.6	6.8 ± 1.0	10.2 ± 1.3	128 ± 35	>800	>800	>600
Kinetic ions	4.4 ± 0.2	5.5 ± 0.2	7.0 ± 0.6	9.2 ± 1.2	10.7 ± 2.0	14.3 ± 2.2	10.5 ± 0.9	13.6 ± 2.2

Note: $\langle\chi_e\rangle$ as a function of the magnetic shear from a sequence of GYRO simulations with a flux-tube cross section of $256\rho_e \times 128\rho_e$ and a binormal resolution $k_{y,max}\rho_e=0.69$ using both adiabatic and kinetic ions. The mass ratio was taken to be $m_i/m_e=400$ in the simulations with kinetic ions. The time average is taken over the interval $2000 L_T/v_{te} < t < 8000 L_T/v_{te}$ in all cases except the adiabatic ion run at $s=0.5$, where the average is taken over $2000 L_T/v_{te} < t < 6200 L_T/v_{te}$ (where this run terminated). The adiabatic ion simulations with $s > 0.5$ all terminated before $t=1000 L_T/v_{te}$. At termination in these simulations, χ_e took on the value indicated in the table.

TABLE IV. DIII-D electron transport analysis.

	$\chi_e/\chi_{e,GB}$	T (keV)	L_T (m)
Fig. 1 and 2, $t=1.82s$, $r/a=0.35$	0.84	3.5	0.17
Figs. 4–6, $r/a=0.35$	0.16	3.5	0.13
Fig. 1 and 2, $t=1.82s$, $r/a=0.6$	10.0	1.5	0.17
Figs. 4–6, $r/a=0.6$	8.6	1.3	0.17

Note: DIII-D transport analysis³⁶ shows $\chi_e, \chi_{e,GB}$ within the internal transport barrier at $r/a=0.35$, while $\chi_e < 10\chi_{e,GB}$ in the L-mode edge plasma ($r/a=0.6$).

ments. These conflicting views can be resolved by calibrating the observed electron heat transport in electron gyro-Bohms and comparing the results to the transport levels observed in the microturbulence simulations of ETG transport reported above. In mks units an electron gyro-Bohm is given by

$$\chi_{e,GB} \equiv \left(\frac{\rho_e}{L_T} \right) \rho_e v_{te} \approx 0.075 [T_e(\text{keV})]^{3/2} [B(T)]^{-2} [L_T(\text{m})]^{-1} \text{ m}^2/\text{s}, \quad (4)$$

where T_e is the electron temperature in keV, B is the magnetic field in Tesla, and L_T is the electron temperature scale length in meters.

The magnitude of the experimentally observed electron thermal conductivity varies with plasma conditions. Of particular interest are discharges with internal transport barriers because the ion-scale turbulence is suppressed by $E \times B$ shear within the barrier while the electron-scale ETG turbulence is largely unaffected by the $E \times B$ shear. Stallard *et al.*³⁶ have analyzed several DIII-D discharges with internal transport barriers. They find the measured electron temperature gradient tracks the (linear) marginally stable gradient for ETG modes within the thermal barrier, suggesting that ETG turbulence controls the electron temperature gradient within these thermal barriers. The electron temperature gradient is substantially larger than the marginally stable gradient in the L-mode edge plasma outside of the thermal barrier, so that ETG modes are strongly unstable in this region and may be responsible for the observed electron heat transport. Table IV presents values of T_e and L_T from Figs. 1–6 of Ref. 36,

together with the experimental electron heat transport calibrated in electron gyro-Bohms both within the thermal barrier and in the L-mode edge.

Inside the internal transport barriers (at $r/a=0.35$ in both discharges) the electron thermal conductivity is less than one electron gyro-Bohm, as one would expect from ETG turbulence near marginal stability. In the L-mode edge plasma (at $r/a=0.6$ for both discharges) the electron thermal conductivity is about 10 electron gyro-Bohms—consistent with our ETG simulation results (with kinetic ions) at high magnetic shear (the magnetic shear at $r/a=0.8$ was $s \approx 1.2$ in both of these discharges). This general pattern is repeated in both JET³⁷ and JT-60U.³⁸ Within the internal transport barrier, $\chi_e/\chi_{e,GB}$ is less than or of the order of 1, rising to values of less than or about 25 in the L-mode plasma outside the barrier.

ETG transport may also be important in NSTX spherical tokamak where transport analysis^{40,41} shows that χ_e is often substantially larger than χ_i and has different variation with the plasma minor radius. This is the case in NSTX shot #108213 at $t=0.3s$, a neutral beam heated L-mode discharge analyzed by Stutman *et al.*⁴⁰ Examining the midradius ($0.3 \leq r/a \leq 0.5$) from Fig. 1(a) of Ref. 40 (see Table V), we find that χ_e is less than $10\chi_{e,GB}$, consistent with our ETG simulation results. Stutman *et al.*⁴⁰ performed a stability analysis at $r/a=0.4$ of shot #108213 at $t=0.3s$ and concluded that ETG modes are linearly unstable in this region. This general behavior ($\chi_e > \chi_i$ with different radial variation) is also seen in high-harmonic fast wave (HHFW) heated L-mode discharges [e.g., shot #106194 at $t=2.43s$ (Ref. 41)] and neutral beam heated H-mode discharges (e.g., shot 112581 at $t=0.55s$ ⁴⁰ and shot #109070 at $t=0.45s$)⁴¹. Reviewing these data, we again find $\chi_e \leq 10\chi_{e,GB}$ at midradius, consistent with our ETG turbulence simulations.

Here we have demonstrated that there are many experiments where the observed value of $\chi_e/\chi_{e,GB}$ is in a range that could be explained by ETG turbulence. Of course this does not rule out that ITG+TEM (trapped electron mode) turbulence might be the dominant source of electron thermal transport in most plasmas. To identify more precisely when ETG is playing a significant role in a particular experiment, it will be necessary to carry out more detailed analysis with self-consistent transport modeling, including the effects of marginal stability and equilibrium-scale sheared flows.

TABLE V. NSTX transport analysis.

	$\chi_e/\chi_{e,GB}$	T (keV)	L_T (m)
shot #1080213@ $t=0.3$ s, $r/a=0.3$	4.4	0.82	0.22
shot #1080213@ $t=0.3$ s, $r/a=0.4$	6.4	0.56	0.15
shot #1080213@ $t=0.3$ s, $r/a=0.5$	7.5	0.48	0.12
shot #112581@ $t=0.55$ s, $r/a=0.7$	6.0	0.46	0.10
shot #106194@ $t=2.43$ s, $R=1.2$ m	7.4	1.02	0.33
shot #109070@ $t=0.45$ s, $R=13.5$ m	10.4	0.80	0.26

Note: Transport analysis from NSTX^{40,41} shows χ_e consistently less than about $10\chi_{e,GB}$ at midradius.

VII. SUMMARY AND CONCLUSIONS

The definition and successful completion of a nonlinear benchmarking exercise is an important step in studying a new regime of plasma microturbulence. We have completed a nonlinear benchmarking of ETG turbulence between four plasma microturbulence codes (GYRO, PG3EQ, GS2, and GENE), achieving agreement in the (time and space) averaged electron thermal transport. The turbulent intensity, correlation functions, turbulent spectra, and rms $E \times B$ flow shear are also in substantial agreement. Our simulation results are shown to be well-converged in time step, velocity-space resolution, parallel grid resolution, and the radial extent of the simulation flux-tube by varying these numerical parameters in the continuum (GYRO) and PIC (PG3EQ) simulation codes. Convergence with respect to resolution in the plane perpendicular to \mathbf{B} is asymmetric. $\langle \chi_e \rangle$ is found to increase with increasing binormal resolution until convergence in binormal resolution is achieved at $k_{y,\max} \rho_e > 1.5$. At fixed binormal resolution, convergence in radial resolution is achieved as the radial resolution approaches the binormal resolution (for runs that are under-resolved in binormal resolution) or $k_{x,\max} \rho_e > 1.5$ (for runs that are converged in binormal resolution). Similarly, $\langle \chi_e \rangle$ is found to increase with increasing binormal flux-tube dimension. The problems of convergence in binormal resolution and binormal flux tube extent discussed in Sec. III will be addressed in future work. In this paper, we have compared results between codes while holding the binormal resolution and flux tube extent constant. The demonstration that continuum and PIC simulations of ETG turbulence achieve a common result when addressing a common operating point should allow community discussion of ETG simulation results to move beyond questions of code accuracy to the physics underlying ETG turbulence. Three such issues addressed here are (i) the structure of the ETG spectrum, (ii) the breakdown of the adiabatic ion model as the magnetic shear is increased beyond $s \approx 0.4$, and (iii) the experimental relevance of the electron heat transport rate observed in simulations of ETG turbulence.

The fluctuation spectrum of ETG turbulence differs from that of ITG turbulence due to the absence of a long-wavelength cutoff in the ETG fluctuation spectrum. Within the adiabatic ion (for ETG) or electron (for ITG) models the linear growth spectra of ETG and ITG are isomorphic so the absence of a long-wavelength cutoff in the ETG fluctuation spectrum must reflect differences in the nonlinear physics of ETG turbulence relative to ITG turbulence. The difference in the adiabatic species response for zonal flows in ITG versus ETG turbulence makes the coupling to zonal flows stronger for ITG turbulence. This stronger coupling is probably responsible for the long-wavelength cutoff observed in the ITG turbulent spectrum. The absence of a long-wavelength cutoff in the ETG turbulent spectrum leads to an increase in the electron heat flux with the binormal extent of the simulation flux tube. It is possible that a realistic magnetic geometry with good flux-surface-averaged curvature will introduce a long-wavelength cutoff through linear damping of long-wavelength ETG modes. In the absence of any long-wavelength cutoff, we can expect that ETG turbulence will

be manifested in experimental measurements of the electron density fluctuation spectrum as a “shoulder” at $k_{\perp} \rho_e \approx 0.15$ on a spectrum that otherwise decreases monotonically from the peak (associated with ion-scale turbulence) in the neighborhood of $k_{\perp} \rho_i \approx 0.2$. The fluctuation spectrum should exhibit a change in the direction of mode propagation from the ion diamagnetic direction at low k_{\perp} ($k_{\perp} \rho_i \leq 0.2$) to the electron diamagnetic direction at higher values of k_{\perp} ($k_{\perp} \rho_e \approx 0.15$). It is our expectation from examining simulations of both ITG and ETG turbulence that there will only be a well-defined frequency at a given value of k_{\perp} below the ITG spectral peak at $k_{\perp} \rho_i \leq 0.2$ and near the ETG shoulder in the spectrum at $k_{\perp} \rho_e \approx 0.15$. We anticipate that it will be difficult to associate a frequency and a direction of propagation to turbulent fluctuations at other values of k_{\perp} .

Within the adiabatic ion model, and for the parameters studied here, there is a dramatic increase in both the intensity of the ETG turbulence and the associated electron heat transport as the magnetic shear is increased beyond $s \approx 0.4$. In the high shear (and high transport) regime, the ETG turbulent spectrum is dominated by the mode with $k_r = 0$ and the lowest nonzero binormal wave number allowed within the cross section of the flux-tube simulation. While this phenomenon is reminiscent of the ETG “streamers” described in the work of Jenko and Dorland,^{13–15} there is an important distinction to be made. The ETG streamers described by Jenko and Dorland were microscopic in the sense that their radial extent could be measured in units of ρ_e , while the ETG streamers seen in our adiabatic ion simulations with $s \geq 0.4$ are macroscopic in the sense that their radial extent is greater than the radial width of the flux tube, going to infinity in the limit $\rho_e^* = \rho_e / a \rightarrow 0$. (Jenko and Dorland’s simulations were with trapped particles turned off, which provides a long-wavelength cutoff in the spectrum and helped their simulations saturate.) The appearance of macroscopic streamers in recent ETG simulations^{11,12,20,21} is also likely an artifact of the adiabatic ion model often employed in simulations of ETG turbulence. The absence of such macroscopic streamers in higher-fidelity simulations of ETG turbulence (e.g., simulations with kinetic ions) bodes well for experimental efforts to detect ETG turbulence employing diagnostics sensitive to fluctuations with a finite radial wave number.

Perhaps the most interesting result of this numerical study of ETG turbulence is the demonstration that ETG turbulence can produce an electron thermal conductivity, $\langle \chi_e \rangle$, as large as $14 (\rho_e / L_T) \rho v_{te}$ —comparable to that obtained by in the limit $r/R_0 \rightarrow 0$ by Jenko and Dorland,^{13–15} and well within the range obtained from transport analyses of tokamak experiments within thermal barriers and in the L-mode edge of many discharges.^{36–38} Similar values of the electron thermal transport are also observed in transport analyses of spherical tokamaks.^{40,41} This demonstration is not conclusive because the simulations in question were not converged in binormal resolution. However, our experience indicates that $\langle \chi_e \rangle$ increases with increasing binormal resolution so these values of $\langle \chi_e \rangle$ probably represent a lower limit. Recent simulations³¹ have found that long-wavelength ITG/TEM turbulence may reduce ETG turbulent intensities and transport levels, so that ETG is more likely to be important in

regimes where the ITG/TEM modes are reduced or have a higher threshold, such as in regimes with hot ions or large equilibrium-scale sheared flows. Hence, this work supports the tentative conclusion that ETG turbulence is a candidate for explaining the electron thermal transport in some tokamak discharges.

ACKNOWLEDGMENTS

We gratefully acknowledge Bruce Cohen for his interest, advice, and careful editing; and Stan Kaye for helpful comments regarding transport analysis on NSTX.

This work was performed under the auspices of the U.S. Department of Energy by Lawrence Livermore National Laboratory under Contract No. W-7405-ENG-48, by Princeton Plasma Physics Laboratory under Contract No. DE-AC02-76CH03073, by the Center for Multiscale Plasma Dynamics at the University of Maryland and UCLA under Contract No. DE-FC02-04ER54784, and at General Atomics under Contracts No. DE-FG03-95ER54309 and No. DE-FG02-92ER54141. The simulations described here made use of resources at the National Energy Research Supercomputer Center under Department of Energy Contract No. DE-AC03-76SF00098.

- ¹B. Coppi and G. Rewoldt, in *Advances in Plasma Physics*, edited by A. Simon and W. B. Thompson (John Wiley and Sons, New York, 1976), Vol. 6, p. 421.
- ²P. N. Guzdar, C. S. Liu, J. Q. Dong, and Y. C. Lee, *Phys. Rev. Lett.* **57**, 2818 (1986).
- ³Y. C. Lee, J. Q. Dong, P. N. Guzdar, and C. S. Liu, *Phys. Fluids* **30**, 1331 (1987).
- ⁴W. Horton, B. G. Hong, and W. M. Tang, *Phys. Fluids* **31**, 2971 (1988).
- ⁵R. E. Waltz, G. D. Kerbel, and J. Milovich, *Phys. Plasmas* **1**, 2229 (1994).
- ⁶B. I. Cohen, D. C. Barnes, J. M. Dawson, G. W. Hammett, W. W. Lee, G. D. Kerbel, J.-N. Leboeuf, P. C. Liewer, T. Tajima, and R. E. Waltz, *Comput. Phys. Commun.* **87**, 1 (1995).
- ⁷A. M. Dimits, T. J. Williams, J. A. Byers, and B. I. Cohen, *Phys. Rev. Lett.* **77**, 71 (1996).
- ⁸A. M. Dimits, G. Bateman, M. A. Beer, B. I. Cohen, W. Dorland, G. W. Hammett, C. Kim, J. E. Kinsey, M. Kotschenreuther, A. H. Kritiz, L. L. Lao, J. Mandrekas, W. M. Nevins, S. E. Parker, A. J. Redd, D. E. Shumaker, R. Sydora, and J. Weiland, *Phys. Plasmas* **7**, 969 (2000).
- ⁹R. E. Waltz, J. Candy, and M. N. Rosenbluth, *Phys. Plasmas* **9**, 1938 (2002).
- ¹⁰B. Labit and M. Ottaviani, *Phys. Plasmas* **10**, 126 (2003).
- ¹¹Z. Lin, L. Chen, Y. Nishimura, H. Qu, T. S. Hahm, J. L. V. Lewandowski, G. Rewoldt, W. X. Wang, P. H. Diamond, C. Holland, F. Zonca, and Y. Li, *Electron Thermal Transport in Tokamaks: ETG or TEM Turbulence?*, Fusion Energy 2004, Proceedings of the 20th Fusion Energy Conference, Vilamoura, 2004 (IAEA, Vienna, 2005), paper TH8.4. See <http://www-naweb.iaea.org/naweb/physics/fec/fec2004/datasets/index.html>.
- ¹²Z. Lin, *On Structures in Electron Temperature Gradient Turbulence*, *Bull. Am. Phys. Soc.* (November, 2004). See <http://www.aps.org/meet/DPP04/baps/index.html>.
- ¹³F. Jenko, W. Dorland, M. Kotschenreuther, and B. N. Rogers, *Phys. Plasmas* **7**, 1904 (2000).
- ¹⁴W. Dorland, F. Jenko, M. Kotschenreuther, and B. N. Rogers, *Phys. Rev.*

- Lett.* **85**, 5570 (2000).
- ¹⁵F. Jenko and W. Dorland, *Phys. Rev. Lett.* **89**, 225001 (2002).
- ¹⁶Y. Idomura, S. Tokuda, and Y. Kishimoto, 2004, *Fusion Energy 2004: Proceedings of the 20th International Conference (Vilamoura, 2004)* (IAEA, Vienna), CD-ROM file TH/8-1 and <http://www-naweb.iaea.org/naweb/physics/fec/fec2004/datasets/index.html>.
- ¹⁷Y. Idomura, S. Tokuda, and Y. Kishimoto, *Nucl. Fusion* **45**, 1571 (2005).
- ¹⁸J. Li and Y. Kishimoto, *Phys. Plasmas* **11**, 1493 (2004).
- ¹⁹J. Q. Li, Y. Kishimoto, N. Miyato, T. Matsumoto, and J. Q. Dong, *Nucl. Fusion* **45**, 1293 (2005).
- ²⁰Z. Lin, L. Chen, and F. Zonca, *Phys. Plasmas* **12**, 056125 (2005).
- ²¹W. M. Nevins, G. W. Hammett, A. M. Dimits, W. Dorland, and D. E. Shumaker, *Phys. Plasmas* **12**, 122305 (2005).
- ²²W. L. Kruer, Report of the June 2005 PSACI PAC meeting (private communication).
- ²³J. Candy and R. E. Waltz, *J. Comput. Phys.* **186**, 545 (2003).
- ²⁴T. S. Hahm, P. H. Diamond, Z. Lin, and S.-I. Itoh, *Plasma Phys. Controlled Fusion* **46**, A323 (2004).
- ²⁵Z. Lin, S. Ethier, T. S. Hahm, and W. M. Tang, *Phys. Rev. Lett.* **88**, 195004 (2002).
- ²⁶J. Candy, R. E. Waltz, and W. Dorland, *Phys. Plasmas* **11**, L25 (2004).
- ²⁷M. N. Rosenbluth and F. L. Hinton, *Phys. Rev. Lett.* **80**, 724 (1998).
- ²⁸P. H. Diamond, S.-I. Itoh, K. Itoh, and T. S. Hahm, *Plasma Phys. Controlled Fusion* **47**, R35 (2005).
- ²⁹Y. Xiao and P. J. Catto, *Phys. Plasmas* **13**, 102311 (2006).
- ³⁰J. Candy, "Coupled ITG/TEM-ETG gyrokinetic simulations," Proceedings of the 21st IAEA Fusion Energy Conference (16–21 October, Chengdu, China) (IAEA, Vienna), paper TH2–1, see <http://www-pub.iaea.org/MTCD/Meetings>; R. E. Waltz, J. Candy, and M. Fahey, "Coupled ITG/TEM-ETG gyrokinetic simulations" *Phys. Plasmas* (submitted).
- ³¹S. Parker, *Bull. Am. Phys. Soc.* **50**, 232 (2005).
- ³²F. Jenko and A. Kendl, *Phys. Plasmas* **9**, 4103 (2002).
- ³³H. Bigrari, P. H. Diamond, and P. W. Terry, *Phys. Fluids B* **2**, 1 (1990).
- ³⁴K. H. Burrell, *Phys. Plasmas* **4**, 1499 (1997).
- ³⁵T. S. Hahm, M. A. Beer, Z. Lin, G. W. Hammett, W. W. Lee, and W. M. Tang, *Phys. Plasmas* **6**, 922 (1999).
- ³⁶B. W. Stallard, C. M. Greenfield, G. M. Staebler, C. L. Rettig, M. S. Chu, M. E. Austin, D. R. Baker, L. R. Bayor, K. H. Burrell, J. C. DeBoo, J. S. DeGrassie, E. J. Doyle, J. Lohr, G. R. McKee, R. L. Miller, W. A. Peebles, C. C. Petty, R. I. Pinsker, B. W. Rice, T. L. Rhodes, R. E. Waltz, L. Zeng, and the DIII-D Team, *Phys. Plasmas* **6**, 1978 (1999).
- ³⁷V. V. Parail, Yu. F. Baranov, C. D. Challis, G. A. Cottrell, B. Fischer, C. Gormezano, G. T. A. Huysmans, X. Litaudon, A. C. C. Sips, F. X. Söldner, E. M. Springmann, A. Taroni, and D. J. Ward, *Nucl. Fusion* **39**, 429 (1999).
- ³⁸H. Shirai, M. Kikuchi, T. Takizuka, T. Fujita, Y. Koide, G. Rewoldt, D. Mikkelsen, R. Budny, W. M. Tang, Y. Kishimoto, Y. Kamada, T. Oikawa, O. Naito, T. Fukuda, N. Isei, Y. Kawano, M. Azumi, and the JT-60 Team, *Nucl. Fusion* **39**, 1713 (1999).
- ³⁹C. C. Petty, M. R. Wade, J. E. Kinsey, D. R. Baker, and T. C. Luce, *Phys. Plasmas* **9**, 128 (2002).
- ⁴⁰D. Stutman, K. W. Hill, M. S. Kaye, M. H. Redi, E. J. Synakowski, M. G. Bell, R. E. Bell, C. Bourdelle, W. Dorland, M. Finkenthal, S. Kubota, B. P. LeBlanc, F. Levington, J. E. Menard, D. R. Mikkelsen, K. Tritz, and the NSTX Team, "Studies of improved electron confinement on NSTX," Proceedings of the 20th IAEA Fusion Energy Conference (1–6 November, 2004, Vilamoura, Portugal) (IAEA, Vienna), paper EX/P2-8, see <http://www-pub.iaea.org/MTCD/Meetings>.
- ⁴¹B. P. LeBlanc, R. E. Bell, S. M. Kaye, D. Stutman, M. G. Bell, M. L. Bitter, C. Bourdelle, D. A. Gates, R. Maingi, S. S. Medley, J. E. Menard, D. Mueller, S. F. Paul, A. L. Roquemore, A. Rosenberg, S. A. Sabbagh, V. A. Soukhanovskii, E. J. Synakowski, J. R. Wilson, and the NSTX Research Team, *Nucl. Fusion* **44**, 513 (2004).